

# Optimal thermodynamic conditions to minimize kinetic by-products in aqueous materials synthesis

Received: 20 December 2022

Accepted: 18 December 2023

Published online: 30 January 2024

 Check for updates

Zheren Wang<sup>1,2,5</sup>, Yingzhi Sun<sup>1,2,5</sup>, Kevin Cruse<sup>1,2</sup>, Yan Zeng<sup>2</sup>, Yuxing Fei<sup>1,2</sup>, Zexuan Liu<sup>3</sup>, Junyi Shangguan<sup>1,2</sup>, Young-Woon Byeon<sup>2</sup>, KyuJung Jun<sup>1,2</sup>, Tanjin He<sup>1,2</sup>, Wenhao Sun<sup>4</sup>✉ & Gerbrand Ceder<sup>1,2</sup>✉

Phase diagrams offer substantial predictive power for materials synthesis by identifying the stability regions of target phases. However, thermodynamic phase diagrams do not offer explicit information regarding the kinetic competitiveness of undesired by-product phases. Here we propose a quantitative and computable thermodynamic metric to identify synthesis conditions under which the propensity to form kinetically competing by-products is minimized. We hypothesize that thermodynamic competition is minimized when the difference in free energy between a target phase and the minimal energy of all other competing phases is maximized. We validate this hypothesis for aqueous materials synthesis through two empirical approaches: first, by analysing 331 aqueous synthesis recipes text-mined from the literature; and second, by systematic experimental synthesis of  $\text{LiIn}(\text{IO}_3)_4$  and  $\text{LiFePO}_4$  across a wide range of aqueous electrochemical conditions. Our results show that even for synthesis conditions that are within the stability region of a thermodynamic Pourbaix diagram, phase-pure synthesis occurs only when thermodynamic competition with undesired phases is minimized.

Over the past decade, the Materials Genome Initiative has made it possible to discover and design new materials from first principles<sup>1–4</sup>. However, synthesizing a computationally predicted material remains a challenging but necessary step before any further investigation into its functional properties<sup>5–7</sup>. Thermodynamic phase diagrams are routinely used to guide scientists to synthesize a target phase by indicating its region of thermodynamic stability<sup>8–11</sup>. However, from a practical experimental perspective, one must carefully optimize reaction conditions to eliminate any undesired competing phases, which often appear as kinetic by-products<sup>12–14</sup>. Traditional phase diagrams do not visualize the free-energy axis, which contains essential information regarding

the thermodynamic competition from these competing phases. Even within the same stability region of a thermodynamic phase diagram, the details of nucleation kinetics can drive a reaction through different intermediate phases<sup>15,16</sup>, which can persist in the final product as undesired by-products.

The difference in free energy between precursors and products is the fundamental driving force that propels a reaction toward thermodynamic equilibrium. The magnitude of the thermodynamic driving force is an effective proxy for phase transformation kinetics, as thermodynamic driving force appears in the kinetic equations of nucleation, diffusion and growth<sup>17–19</sup>. Here we hypothesize that one avenue to

<sup>1</sup>Department of Materials Science & Engineering, University of California, Berkeley, Berkeley, CA, USA. <sup>2</sup>Materials Sciences Division, Lawrence Berkeley National Laboratory, Berkeley, CA, USA. <sup>3</sup>Industrial Enterprise & Systems Engineering, University of Illinois at Urbana-Champaign, Urbana, IL, USA.

<sup>4</sup>Department of Materials Science and Engineering, University of Michigan, Ann Arbor, MI, USA. <sup>5</sup>These authors contributed equally: Zheren Wang, Yingzhi Sun. ✉ e-mail: [whsun@umich.edu](mailto:whsun@umich.edu); [gceder@berkeley.edu](mailto:gceder@berkeley.edu)

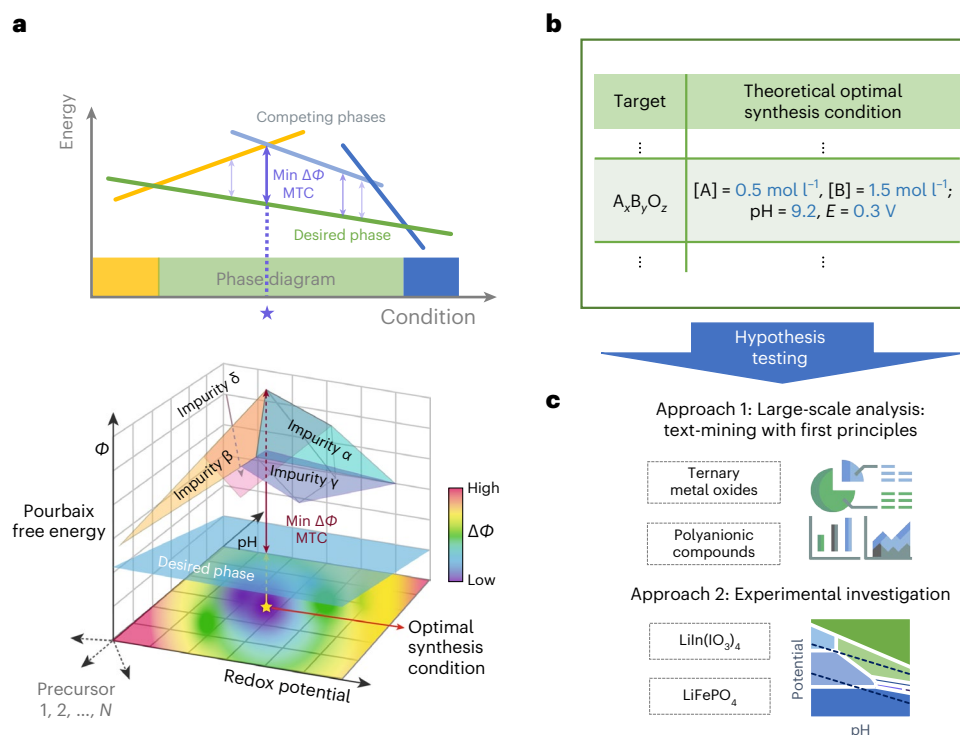


**Fig. 1 | Schematic representation of approach for predicting aqueous-solution-based synthesis conditions.** **a**, Generation of the hypothesis: conditions where the target phase experiences minimum thermodynamic competition from other phases are favoured for synthesis. Upper: the 2D plot depicts this general concept. The different coloured lines represent the energy of various phases. The green line represents the desired target phase; the other lines depict the energies of competing phases. Double-headed arrows between the lines illustrate the difference in free energy between the desired target phase and the minimum free energy among all competing phases, which is the thermodynamic competition denoted as  $\Delta\Phi$ . The solid arrow indicates the

MTC, and stars denote the conditions at which MTC is achieved. The projection of the phases with the lowest energy under different conditions forms the thermodynamic phase diagram, with the stability regions of phases indicated by blocks of corresponding colours. Lower: the 3D plot represents the energy landscape of thermodynamic competition in a multidimensional Pourbaix system. The dotted line axes represent the high-dimensional aspect for the other conditions. **b**, Predictive synthesis: minimizing thermodynamic competition to predict synthesis conditions.  $E$ , redox potential. **c**, Hypothesis testing: large-scale analysis based on the text-mined dataset and detailed investigation of  $\text{LiIn}(\text{IO}_3)_4$  and  $\text{LiFePO}_4$ .

determine optimal synthesis conditions is to maximize the difference in relative free energy between a target phase and its competing phases, as illustrated in Fig. 1a. When the free energy difference between a target phase and its competing phases is maximized, there will be a large difference in relative driving force from the precursor to target phase versus precursor to by-product phases, meaning the likelihood that kinetic factors can promote the competing phases is reduced. We name this hypothesis ‘minimum thermodynamic competition’ (MTC). Importantly, this identifies a unique point in thermodynamic space for optimal materials synthesis, such as the example in Fig. 1b—in contrast with a stability region from the thermodynamic phase diagram. A similar concept based on maximum driving force was recently proposed by Walters and Rondinelli for determination of which oxide phases form to protect against metal corrosion<sup>20</sup>.

Here we present an optimization strategy that relies on the inherent concave geometry of the free-energy landscape of an aqueous electrochemical system (see Methods section), which leads to an efficient computational algorithm that can be readily scaled to high-dimensional (multicomponent) optimization spaces<sup>21</sup>. We provide empirical confirmation of our MTC hypothesis using two complementary approaches, as shown in Fig. 1c. First, we perform a large-scale analysis on a text-mined dataset of solution synthesis recipes<sup>22</sup>, and find that within the available parameter space of synthesis conditions, the experimentally reported (and probably optimized) synthesis conditions lie near the conditions predicted by our MTC criteria. Second, we perform a detailed thermodynamic competition analysis of two systems,  $\text{LiIn}(\text{IO}_3)_4$  and  $\text{LiFePO}_4$ , and confirm by systematic experimental

investigations that the desired target materials can only be synthesized in phase-pure form when the thermodynamic competition is minimized. Our work illustrates how a comprehensive understanding of the free-energy axis of a phase diagram, considering not only the stable phase but also its competing phases, enables the computational design and guidance of optimal materials synthesis conditions.

## Thermodynamic competition in aqueous-solution-based systems

Our thermodynamic strategy aims to maximize the thermodynamic driving force from precursors to the desired target while minimizing that to the competing phases, thus leading to synthesis conditions that maximize the chance of obtaining high phase purity while avoiding the kinetic formation and persistence of competing products. When considering the stability of a target material, the thermodynamic boundary conditions should be framed to examine the stability response of the target material with respect to an open external chemical reservoir. In such case, the natural variables of the thermodynamic system are intensive, and the resulting free-energy surfaces are concave. This transforms the conditions of heterogeneous equilibrium from a convex hull—which applies to extensive variables such as composition—to a concave envelope, which can be solved by half-space intersection<sup>15,23</sup>.

From this geometric description of the energy landscape, the thermodynamic competition that a target phase experiences from the other phases is defined as the difference in free energy between the desired target phase and the minimum free energy of all competing phases, and is schematically shown in Fig. 1a. We denote phase  $k$

as the desired target phase,  $Y$  as intensive variables and  $I_c$  as the index set of other competing phases. The thermodynamic competition that the phase  $k$  experiences from other phases,  $\Delta\Phi(Y)$ , can be written as:

$$\Delta\Phi(Y) = \Phi_k(Y) - \min_{i \in I_c} \Phi_i(Y) \quad (1)$$

Here  $\Phi_k(Y)$  is the free energy of the desired target phase, and  $\min_{i \in I_c} \Phi_i(Y)$  is the minimum free energy of all competing phases. Note that for multiple intensive variables,  $Y$  represents a multidimensional vector rather than a scalar.

As  $\Delta\Phi_k(Y)$  decreases, the thermodynamic competition that the desired target phase experiences with other phases becomes weaker. Thus, the condition where the thermodynamic competition that phase  $k$  experiences is minimized is written as:

$$Y^* = \underset{Y}{\operatorname{argmin}} \Delta\Phi(Y) = \underset{Y}{\operatorname{argmin}} \left[ \Phi_k(Y) - \min_{i \in I_c} \Phi_i(Y) \right] \quad (2)$$

According to our proposed definition, the  $\Delta\Phi$  for a thermodynamically stable phase is always negative, indicating that the target compound possesses a lower free-energy state than all its competing phases. Minimizing the thermodynamic competition with undesired phases is equivalent to maximizing the energy difference from the most competitive competing phase to the target phase.

To model solid–aqueous equilibrium, the Pourbaix potential,  $\Psi$ , provides the free-energy surfaces needed to compute the thermodynamic competition that the desired target phase experiences from its competing phases in the aqueous solution. As we previously derived in ref. 15, the Pourbaix potential is written as:

$$\begin{aligned} \bar{\Psi} = & \frac{1}{N_M} ((G - N_O \mu_{H_2O}) - RT \times \ln(10) \times (2N_O - N_H) \text{pH} \\ & - (2N_O - N_H + Q)E) \end{aligned} \quad (3)$$

where  $N_M$ ,  $N_O$  and  $N_H$  are the number of metal, oxygen and hydrogen atoms in the composition, respectively;  $Q$  is the charge of the phase;  $R$  is the ideal gas constant;  $T$  is the temperature; and  $E$  is the redox potential. The molar Gibbs free energy of a substance,  $G$ , is its chemical potential given by,  $\mu_i = \mu_i^\circ + RT \ln[a_i]$ , where  $\mu_i^\circ$  is given by the standard-state Gibbs formation free energy and  $a_i$  is the activity. For solids, the activity is 1, whereas for ions, the activity scales with the aqueous metal ion concentration. Here we assume that the aqueous solution is ideal, such that  $a_i = x_i$ .

From our MTC framework, the intensive variables  $Y$  in aqueous materials synthesis are pH,  $E$  and the concentrations of the metal ions. For an aqueous system with three metal ions, this becomes a five-dimensional optimization space. In Supplementary Information Note 1, we provide a gradient-based computational algorithm that efficiently identifies the optimal point within the five-dimensional thermodynamic space. There are three additional considerations for the MTC framework. (1) In aqueous synthesis, we assume that diffusion and growth are fast and that nucleation is the rate-limiting step in phase transformation kinetics. The MTC analysis determines which phase has the largest driving force to nucleate, based on the initial experimentally prepared solution conditions. Although large differences in surface energies can promote the preferential nucleation of metastable phases<sup>24–26</sup>, we will show here that large free-energy differences between the target and competing phases can effectively overcome the fast nucleation or long persistence of metastable intermediates. (2) Following nucleation, growth of the solid phases will consume ions in solution thereby changing the concentrations, pH and redox potential<sup>16</sup>. In principle, this can be addressed by developing a model that calculates these changes from the amount of solid materials formed and re-evaluates the Pourbaix potential for the changing conditions<sup>15</sup>. (3) Our MTC metric here does not consider the influence of temperature

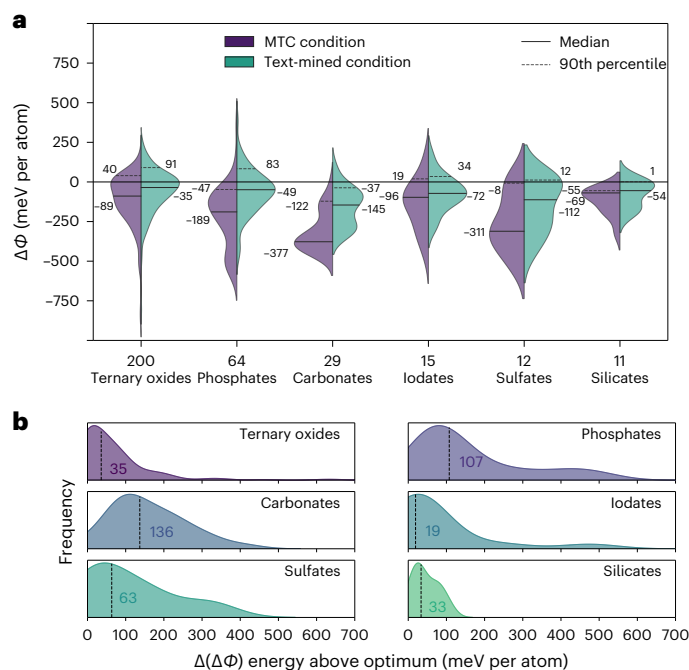


**Fig. 2 | Thermodynamic competition analysis on text-mined dataset.**

**a**, Gaussian kernel density estimates of thermodynamic competition distributions of different multicomponent functional oxides. **b**, Gaussian kernel density estimates of the thermodynamic competition differences of different compounds between the text-mined conditions and their corresponding thermodynamically optimal conditions. The highlighted number is the median for all entries.

or time. Aqueous synthesis tends to occur at relatively low synthesis temperatures (generally  $\leq 250$  °C even under hydrothermal conditions) as compared to solid-state powder synthesis (up to  $\sim 1,000$  °C); under our aqueous synthesis conditions, we thus assume that the contribution of  $\Delta S$  ( $\Delta S$  being the change in entropy between different phases) away from 25 °C, where the original Pourbaix formalism was fitted<sup>27</sup>, is small relative to the  $\mu^\circ$  term in our stability and driving-force analyses. The MTC analysis also does not consider time, as our analyses aim to predict structure selection at the instant of nucleation, whereas longer-time considerations are more relevant in modelling crystal growth and particle morphology.

## Evaluation of MTC from literature aqueous synthesis recipes

Recently, we used a variety of natural-language-processing algorithms to text-mine 35,675 solution synthesis recipes from the literature<sup>22</sup>. Here we combine this dataset with first-principles multielement Pourbaix diagrams from the Materials Project<sup>3,27</sup> to interrogate our MTC hypothesis. When optimizing a solution synthesis procedure, there are many experimental degrees of freedom available—including precursor selection, precursor molar concentration, pH and redox potential. We will show that the majority of literature-reported solution synthesis conditions are near the optimal conditions as predicted by MTC, providing post hoc empirical validation of the MTC hypothesis.

In the Methods, we describe the procedure for converting a reported synthesis recipe into metal ion concentrations, pH values and effective redox potential, and the calculation of thermodynamic competition under given text-mined conditions. Our text-mined dataset contains 331 synthesis recipes, including recipes for 200 ternary metal oxides, 64 phosphates, 29 carbonates, 15 iodates, 12 sulfates and 11 silicates.

**Table 1 | Synthesis parameters with thermodynamic competition analysis and experimental results from X-ray diffraction measurements for the synthesis of  $\text{LiIn}(\text{IO}_3)_4$** 

ID	Lithium source	[Li]	[In]	[I]	pH	$E$ (V)	$\Delta\Phi$ (meV per atom)	X-ray diffraction results
A1	$\text{LiCl} + \text{Li}(\text{CH}_3\text{COO})$	1.5	0.1	0.8	0.77	1.58	-58	$\text{LiIn}(\text{IO}_3)_4$
A2	$\text{LiCl}$	1.5	0.1	0.8	0.66	1.59	-56	$\text{LiIn}(\text{IO}_3)_4$
A3	$\text{LiCl} + \text{Li}(\text{CH}_3\text{COO})$	1.2	0.1	0.8	0.56	1.59	-51	$\text{LiIn}(\text{IO}_3)_4$
A4	$\text{LiCl}$	1.2	0.1	0.8	0.43	1.60	-46	$\text{In}(\text{IO}_3)_3$
A5	$\text{LiCl} + \text{Li}(\text{CH}_3\text{COO})$	0.8	0.1	0.8	0.87	1.57	-15	$\text{In}(\text{IO}_3)_3$
A6	$\text{LiCl}$	0.8	0.1	0.8	0.71	1.58	-13	$\text{In}(\text{IO}_3)_3$
A7	$\text{LiCl} + \text{Li}(\text{CH}_3\text{COO})$	0.5	0.1	0.8	0.65	1.59	-11	$\text{In}(\text{IO}_3)_3$
A8	$\text{LiCl}$	0.5	0.1	0.8	0.52	1.60	-9	$\text{In}(\text{IO}_3)_3$
A9	$\text{Li}(\text{CH}_3\text{COO})$	0.15	0.1	0.8	0.91	1.57	-8	$\text{In}(\text{IO}_3)_3$
A10	$\text{LiCl}$	0.15	0.1	0.8	0.85	1.58	-8	$\text{In}(\text{IO}_3)_3$

The concentrations are reported in molarity ( $\text{mol l}^{-1}$ ), calculated with the assumption that all the precursors are completely dissociated. The specific amount of precursors can be found in Methods. The pH values are experimentally measured. The redox potentials are derived from data in Pourbaix's Atlas<sup>40</sup>.

First, we confirm that the majority of the materials in our text-mined dataset are stable phases on the Pourbaix diagram under some thermodynamic condition, in other words  $\Delta\Phi \leq 0$ . Specifically, Pourbaix-stable phases account for 125/200 ternary metal oxides, 47/64 phosphates, 27/29 carbonates, 11/15 iodates, 8/12 sulfates and 9/11 silicates. In Fig. 2a, we plot the distributions of thermodynamic competition,  $\Delta\Phi$ , for both the MTC-predicted thermodynamic optimal conditions (left violin plot) versus the reported text-mined synthesis conditions (right violin plot), using kernel density estimates (KDEs) of the thermodynamic competition distributions for ternary metal oxides and different polyanionic compounds.

Given the fact that these materials have been synthesized, we can directly estimate the magnitude of the MTC that may be required to synthesize materials in aqueous solutions. We find that ternary metal oxides have a median  $\Delta\Phi = -89$  meV per atom, phosphates at  $\Delta\Phi = -189$  meV per atom, carbonates at  $\Delta\Phi = -377$  meV per atom, iodates at  $\Delta\Phi = -96$  meV per atom, sulfates at  $\Delta\Phi = -311$  meV per atom and silicates at  $\Delta\Phi = -69$  meV per atom. Because these values are derived from reported successful syntheses, they may serve as guidelines when evaluating the aqueous synthesizability of novel computationally predicted materials.

Whereas Fig. 2a shows overall distributions between the thermodynamically optimal conditions and the text-mined condition distributions, Fig. 2b shows for specific compounds the one-to-one difference in energy between their text-mined thermodynamic conditions and the corresponding MTC-predicted optimal conditions. Hereinafter, we refer to this difference in experimental versus theoretically optimal energy difference as  $\Delta(\Delta\Phi)$  or the 'energy above optimum'.

Figure 2b shows that text-mined reported procedures are slightly non-optimal, which is evidenced by the peak in probability distribution at  $\Delta(\Delta\Phi)$  being slightly above the MTC-predicted optimal conditions. There are multiple reasons for this. First, successful synthesis of a phase-pure target is not limited to the MTC optimum. Once a synthesis route has been developed for a material, researchers may not feel the need to explore all other possible conditions<sup>28</sup>. Stated in more mathematical language, the optimization function of experimental work (achieving a phase-pure target in a reasonable time) is not identical to the MTC function. Any contribution to the data from successful reactions away from the MTC (which is a single point in parameter space) leads by definition to a positive contribution to  $\Delta(\Delta\Phi)$ . A second reason is that experimental constraints, not included in our analysis, make synthesis under some conditions less desirable. For example, extreme pH or oxidation potential values may create safety or containment hazards<sup>29</sup>. It is further possible that density functional theory (DFT)

formation energy errors, which are of the order of 25 meV per atom (ref. 30), can lead to inaccuracies in specific  $\Delta(\Delta\Phi)$  systems. Nevertheless, the magnitude of  $\Delta(\Delta\Phi)$  (medians ranging from 19 to 136 meV per atom) is much smaller than the magnitude of thermodynamic competition (medians ranging from -69 to -377 meV per atom) shown in Fig. 2a, which suggests that the experimentally optimized conditions are near the thermodynamically optimal conditions. Most importantly, this provides a large-scale empirical validation that the MTC predicts synthesis conditions that are likely to be experimentally viable.

A final intriguing observation from Fig. 2a is that many synthesized materials have text-mined  $\Delta\Phi$  values that are positive, suggesting that some compounds can be synthesized under conditions where they are not the lowest free-energy phase. For example, the 90th percentile boundary is  $\Delta\Phi = +83$  meV per atom for phosphates and +34 meV per atom for iodates. This compares closely to the 90th percentile of inorganic crystalline metastability, which was previously reported to be ~67 meV per atom energy above the convex hull averaged across many chemistries<sup>31</sup>. It is well understood that the relatively low temperatures of solution synthesis often allow 'chimie douce' kinetics<sup>32</sup> to dominate structure selection during nucleation<sup>33,34</sup>, which may facilitate the formation of metastable compounds. Our text-mined dataset provides explicit quantitative validation of this anecdotal intuition for the realization of metastable materials.

Overall, our text-mined dataset provides explicit post hoc empirical validation of the MTC hypothesis, and furthermore highlights the value of such text-mined datasets in not only providing data to train machine-learning models<sup>35</sup>, but also in empirically validating new mechanistic theories<sup>36</sup>.

### MTC-guided aqueous synthesis of $\text{LiIn}(\text{IO}_3)_4$ and $\text{LiFePO}_4$

In addition to our text-mined dataset validation of the MTC hypothesis, we also directly validate the MTC hypothesis by evaluating its ability to guide the experimental synthesis of multicomponent oxides. Here we apply the MTC to search for optimal aqueous electrochemical conditions to synthesize  $\text{LiIn}(\text{IO}_3)_4$ , a promising superionic conductor<sup>37</sup>, and  $\text{LiFePO}_4$ , a commercialized cathode material<sup>38</sup>. This represents two five-dimensional thermodynamic spaces in which to find optimized conditions, which are  $[\text{Li}]-[\text{In}]-[\text{I}]-\text{pH}-E$  for  $\text{LiIn}(\text{IO}_3)_4$  and  $[\text{Li}]-[\text{Fe}]-[\text{P}]-\text{pH}-E$  for  $\text{LiFePO}_4$ . We will show that only conditions with  $\Delta\Phi \leq -51$  meV per atom and  $\Delta\Phi \leq -29$  meV per atom successfully result in phase-pure  $\text{LiIn}(\text{IO}_3)_4$  and  $\text{LiFePO}_4$ , respectively. The magnitudes of these  $\Delta\Phi$  values are consistent with our data-driven analyses from our text-mined recipes. This  $\Delta\Phi$  information is inaccessible from traditional



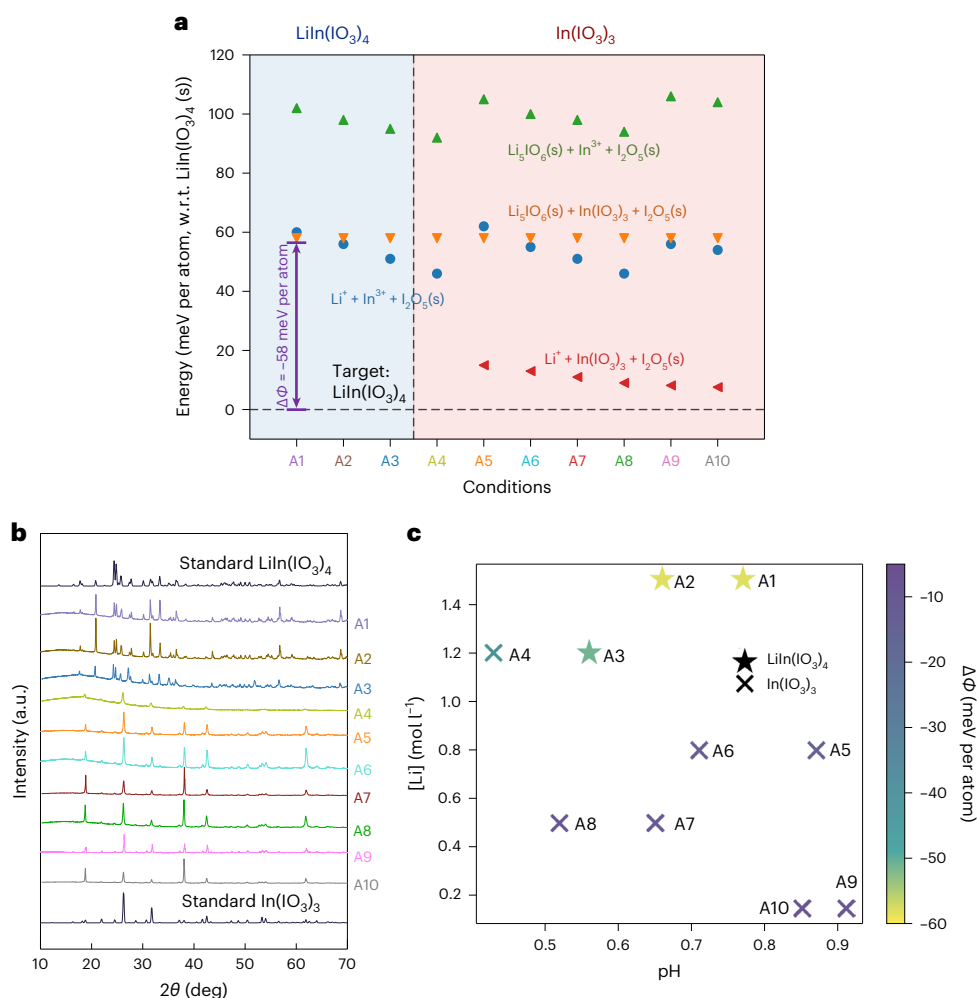


**Fig. 3 |  $\text{LiIn}(\text{IO}_3)_4$  thermodynamic competition analysis and the corresponding synthesis results. a**, The Pourbaix potentials of common competing phases with respect to the energy of  $\text{LiIn}(\text{IO}_3)_4$  under conditions A1–A10. The MTC is the negative of the lowest energy of competing reactions. The blue and red shading represent  $\text{LiIn}(\text{IO}_3)_4$  and  $\text{In}(\text{IO}_3)_3$ , respectively, observed as final products under regions of synthesis conditions. **b**, X-ray diffraction results for syntheses under conditions A1–A10, which are associated with varying

lithium concentration, pH and redox potential. **c**, Scatter plot representing the thermodynamic competition with respect to pH, redox potential and lithium concentration for the synthesis of  $\text{LiIn}(\text{IO}_3)_4$ . The redox potential is calculated using  $E^\ominus(\text{H}_5\text{IO}_6/\text{HIO}_3) = 1.626$  V (refs. 40,41). Each scatter point represents one of conditions A1–A10. The stars indicate successful trials (A1–A3), where  $\text{LiIn}(\text{IO}_3)_4$  was successfully synthesized. The crosses indicate failed trials (A4–A10), where  $\text{In}(\text{IO}_3)_3$  was formed as the final product.

Pourbaix diagrams, which only show the stability region and do not provide the conditions for optimal phase selectivity.

### $\text{LiIn}(\text{IO}_3)_4$ synthesis analysis

First, we focused on synthesizing phase-pure  $\text{LiIn}(\text{IO}_3)_4$ , which was predicted to exhibit one of the highest room-temperature lithium ionic conductivities, reaching up to  $18$   $\text{mS cm}^{-1}$  in the pristine state<sup>37</sup>. When we attempted to reproduce the synthesis of this material using the published procedure from Yang et al.<sup>39</sup>, we were unable to produce the target compound. However, using the MTC, we were able to identify robust synthesis conditions that led to the successful synthesis of  $\text{LiIn}(\text{IO}_3)_4$ .

MTC indicates that the most competitive phase (that is, the phase with the lowest energy among all competing phases) is  $\text{In}(\text{IO}_3)_3$ . The MTC analysis further suggests that to promote  $\text{LiIn}(\text{IO}_3)_4$ , we should maximize the aqueous concentration of lithium, and drive the solution towards a highly oxidizing and acidic environment. We can rationalize this prediction because increasing the concentration of  $\text{Li}^+$  increases the supersaturation of  $\text{LiIn}(\text{IO}_3)_4$ , while it has no effect on the competitive non-lithium-bearing phase  $\text{In}(\text{IO}_3)_3$ . The oxidizing environment is

required because the polyanion  $\text{IO}_3^-$  can only exist at a high redox potential because the standard half-cell potential for decomposition to  $\text{I}_2$  is  $E^\ominus(\text{IO}_3^-/\text{I}_2(\text{s})) = 1.18$  V. Simultaneously, an acidic environment is required to avoid hydrolysis of  $\text{In}^{3+}$  to phases such as  $\text{InOOH}$ . Following the MTC recommendations, we designed a series of synthesis experiments that spanned a range of  $\Delta\Phi$  to evaluate the predictive power of the MTC analysis.

The highly oxidizing and acidic environment was created by using an  $\text{H}_5\text{IO}_6$  ( $E^\ominus(\text{H}_5\text{IO}_6/\text{HIO}_3) = 1.626$  V)<sup>40,41</sup> precursor as the iodine source. The experimental synthesis conditions and corresponding thermodynamic competition and final products are given in Table 1. The effective redox potential of  $\text{H}_5\text{IO}_6$  as a function of pH is given by the Nernst equation (Methods).

Condition A9 replicates the condition reported by Yang et al.<sup>39</sup>, in which  $\text{Li}(\text{CH}_3\text{COO})$  is used as the lithium source, achieving  $[\text{Li}] = 0.15$   $\text{mol l}^{-1}$ . Additional experiments were designed with varying lithium concentrations, ranging from  $0.5$  to  $1.5$   $\text{mol l}^{-1}$ , all using  $\text{Li}(\text{CH}_3\text{COO})$  as the lithium source. Detailed results for these experiments are provided in Supplementary Information Note 2. We confine our MTC investigation here to the low-pH regime because we found that

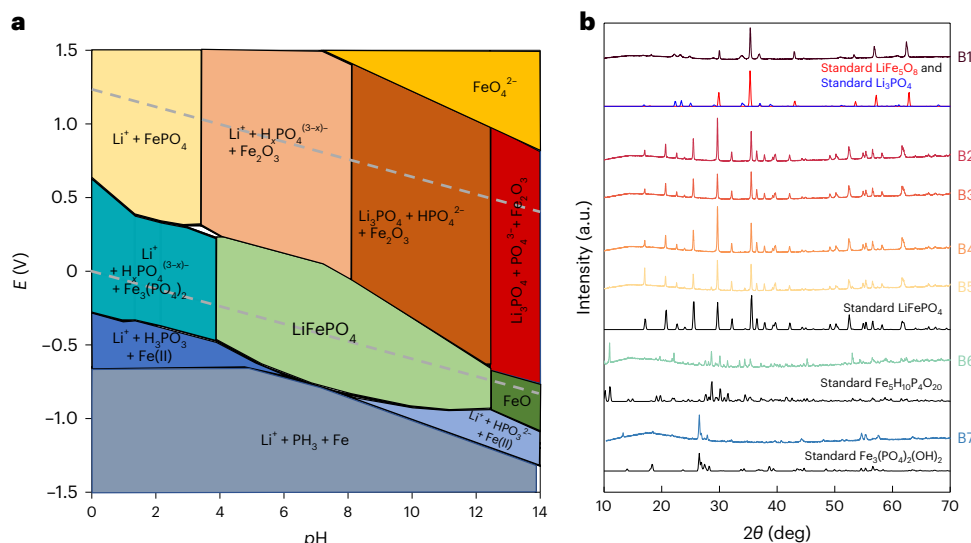


**Fig. 4 | Pourbaix diagram of the Li–Fe–P–H<sub>2</sub>O system and synthesis results.** **a**, Li–Fe–P–H<sub>2</sub>O Pourbaix diagram with [Li] = 0.75 mol l<sup>-1</sup>, [Fe] = 0.25 mol l<sup>-1</sup>, [P] = 0.3 mol l<sup>-1</sup>. The stability regions of different stable phases are marked in

different colours. **b**, X-ray diffraction results on the products from syntheses under conditions B1–B7, which are associated with varying phosphorus concentration, pH and redox potential.

for  $\text{pH} \geq 1.27$  ( $[\text{Li}] \geq 0.5 \text{ mol l}^{-1}$ ) the  $\text{In}_2\text{O}_3$  precursor does not fully dissolve, leading to uncertainty as to what the indium concentration is. To increase the lithium concentration and maintain  $\text{pH} \leq 1$ , we employed LiCl as an alternative lithium source, as the presence of  $\text{CH}_3\text{COO}^-$  would act as a pH buffer, which would have increased pH from the desired highly acidic solution. Condition A1 is the optimal condition predicted by the MTC, achievable by utilizing both LiCl and  $\text{Li}(\text{CH}_3\text{COO})$  as the sources of lithium. Condition A2 is designed to be similar to A1 but utilizes solely LiCl as the lithium source.

To further investigate the influence of lithium concentration and pH, conditions A3–A8 and A10 are designed with intermediate lithium concentrations, using LiCl and an  $\text{Li}(\text{CH}_3\text{COO})/\text{LiCl}$  mixture as the lithium source, respectively.

$\text{LiIn}(\text{IO}_3)_4$  was successfully synthesized under conditions A1–A3, whereas  $\text{In}(\text{IO}_3)_3$  was the product phase for conditions A4–A10. Figure 3a shows the Pourbaix potentials of several competitive phases with respect to  $\text{LiIn}(\text{IO}_3)_4$  under conditions A1–A10, and Fig. 3b presents the X-ray diffraction results of the corresponding syntheses. The XRD data of standard  $\text{LiIn}(\text{IO}_3)_4$  and  $\text{In}(\text{IO}_3)_3$  refer to ICSD-422056 and ICSD-250450 (ICSD release 2023.1), respectively<sup>42</sup>. Figure 3c directly maps the lithium concentrations, pH and redox potential to  $\Delta\Phi$  to the corresponding synthesis products under conditions A1–A10.

In line with the MTC theory, our experiments confirm that the more negative  $\Delta\Phi$ , the higher the kinetic propensity to synthesize a phase-pure material. Importantly, we find that even within the Pourbaix stability region of  $\text{LiIn}(\text{IO}_3)_4$ , where  $\Delta\Phi < 0$ , impurity phases can form when the  $\Delta\Phi$  relative to the target phase is not negative enough. Under conditions A1–A3, with  $\Delta\Phi < -51 \text{ meV per atom}$ , implying limited thermodynamic competition from other phases,  $\text{LiIn}(\text{IO}_3)_4$  can be readily synthesized. Even though under conditions A4–A10  $\text{LiIn}(\text{IO}_3)_4$  is still the stable phase as indicated by a negative  $\Delta\Phi$  (–8 to –46 meV per atom), the energetic proximity of undesired phases means that various kinetic mechanisms may drive their more favourable formation. Experimentally,  $\text{In}(\text{IO}_3)_3$  is the final product of conditions A4–A10, which complements the finding from thermodynamic competition analysis that  $\text{In}(\text{IO}_3)_3$  is the most competitive phase under conditions A5–A10, and the second most competitive phase under condition A4, as shown in Fig. 3a.

Our successful synthesis of  $\text{LiIn}(\text{IO}_3)_4$  under conditions A1 and A2 indicates that the irreproducibility of the experiment from Yang et al. (corresponding to our A9 condition) can be due to human error, as

Yang et al. reported  $[\text{Li}] = 0.15 \text{ mol l}^{-1}$  instead of an actual optimal concentration of  $[\text{Li}] = 1.5 \text{ mol l}^{-1}$ . MTC not only predicts robust synthesis conditions to synthesize  $\text{LiIn}(\text{IO}_3)_4$ , but can also provide a sanity check to verify literature synthesis recipes—overall providing a valuable tool to guide synthesis design.

#### LiFePO<sub>4</sub> synthesis analysis

In our second example, we evaluate the MTC for providing the precise conditions for successful phase-pure synthesis of  $\text{LiFePO}_4$ . The Pourbaix diagram shown in Fig. 4a presents the stable phases in the Li–Fe–P–H<sub>2</sub>O aqueous electrochemical system at ion concentrations of  $[\text{Li}] = 0.75 \text{ mol l}^{-1}$ ,  $[\text{Fe}] = 0.25 \text{ mol l}^{-1}$ ,  $[\text{P}] = 0.3 \text{ mol l}^{-1}$ .  $\text{LiFePO}_4$  is stable only in the near-neutral pH region. (Note that  $\text{LiFePO}_4$  is not Pourbaix-stable at conventional Pourbaix ion concentrations of  $[\text{M}] = 10^{-6} \text{ mol l}^{-1}$ ; this illustrates that it is not appropriate to evaluate electrochemical stability or metastability without considering ion concentrations that are above the solubility product of a target phase<sup>43</sup>).

Results reported by Liu et al.<sup>44</sup> indicate that  $\text{LiFePO}_4$  was not successfully synthesized even within this thermodynamically stable region. Here we experimentally validate that the MTC identifies the optimal conditions within the  $\text{LiFePO}_4$  stability window to successfully produce phase-pure  $\text{LiFePO}_4$ .

Table 2 summarizes the concentrations of lithium, iron and phosphorus, the pH, the redox potential and the final products under different synthesis conditions, which span the experimental conditions used by Liu et al.<sup>44</sup>. Various amounts of  $\text{H}_3\text{PO}_4$  were used to control the pH and the phosphorus concentration. The pH values in Table 2 are measured values, whereas the redox potentials are estimated based on glucose oxidation ( $E^\ominus(\text{CO}_2/\text{C}_6\text{H}_{12}\text{O}_6) = -0.016 \text{ V}$ )<sup>45</sup>, which comes from the hydrolysis of sucrose, acting as a reducing agent in this system. The effective redox potential of glucose as a function of pH is given by the Nernst equation (Methods). Figure 4(b) presents the X-ray diffraction results for the products synthesized under conditions B1–B7, indicating that  $\text{LiFePO}_4$  is successfully synthesized under conditions B2–B5. By contrast,  $\text{LiFePO}_4$  does not form under basic condition B1 or acidic conditions B6 and B7—even though the pH for B6 is within the Pourbaix stability region for  $\text{LiFePO}_4$ . Here the XRD data of standard  $\text{Li}_3\text{PO}_4$ ,  $\text{LiFe}_3\text{O}_8$ ,  $\text{LiFePO}_4$ ,  $\text{Fe}_3\text{H}_{10}\text{P}_4\text{O}_{20}$  and  $\text{Fe}_3(\text{PO}_4)_2(\text{OH})_2$  refer to ICSD-10257, ICSD-35768, ICSD-15448, ICSD-61695 and ICSD-91881 (ICSD release 2023.1), respectively<sup>42</sup>.

**Table 2 | Synthesis parameters with thermodynamic competition analysis and experimental results for LiFePO<sub>4</sub> synthesis**

ID	[Li]	[Fe]	[P]	pH	<i>E</i> (V)	$\Delta\Phi$ (meV per atom)	Product
B1	0.75	0.25	0.15	12.35	-0.74	1	LiFe <sub>2</sub> O <sub>8</sub> and Li <sub>3</sub> PO <sub>4</sub>
B2	0.75	0.25	0.27	9.27	-0.56	-71	LiFePO <sub>4</sub>
B3	0.75	0.25	0.28	8.29	-0.50	-58	LiFePO <sub>4</sub>
B4	0.75	0.25	0.29	7.21	-0.44	-43	LiFePO <sub>4</sub>
B5	0.75	0.25	0.44	6.00	-0.37	-29	LiFePO <sub>4</sub>
B6	0.75	0.25	0.69	5.13	-0.31	-19	Fe <sub>5</sub> H <sub>10</sub> P <sub>4</sub> O <sub>20</sub>
B7	0.75	0.25	1.82	0.95	-0.07	44	Fe <sub>3</sub> (PO <sub>4</sub> ) <sub>2</sub> ·3H <sub>2</sub> O

The concentrations are reported in molarity (mol l<sup>-1</sup>), calculated on the assumption that all the precursors are completely dissociated. The specific amount of precursors can be found in Methods. The pH values are experimentally measured. The redox potentials are estimated based on glucose oxidation<sup>45</sup>.

We calculated  $\Delta\Phi$  for the seven experimental conditions (B1–B7) and found that thermodynamic stability ( $\Delta\Phi \leq 0$ ) is not a sufficient predictor for the formation of phase-pure LiFePO<sub>4</sub>. Similar to our findings for LiIn(IO<sub>3</sub>)<sub>4</sub> synthesis, LiFePO<sub>4</sub> can only be synthesized when  $\Delta\Phi \leq -29$  meV per atom, indicating minimal thermodynamic competition from potential impurity phases. As the pH changes from basic to acidic, the thermodynamic competition first decreases and then increases, with the resulting product phases agreeing well with the thermodynamic predictions. Under condition B1, when the pH is 12.35,  $\Delta\Phi = +1$  meV per atom, and therefore the thermodynamic competition LiFePO<sub>4</sub> experiences from other phases is very strong and LiFePO<sub>4</sub> is not the stable phase, which explains why LiFePO<sub>4</sub> was not the final product under this condition.

As the pH decreases to neutral and weak acidic regions (conditions B2–B5), the  $\Delta\Phi$  ranges from -71 to -29 meV per atom, and therefore LiFePO<sub>4</sub> is not only the stable equilibrium phase, but also experiences minimal thermodynamic competition. LiFePO<sub>4</sub> was successfully synthesized as the final product under all these conditions. However, as the pH further decreases to 5.13 (condition B6), the  $\Delta\Phi$  reduces in magnitude to -19 meV per atom, and therefore the relative energy of the competing phases becomes closer to that of LiFePO<sub>4</sub>, resulting in greater thermodynamic competition than that under conditions B2–B5. Accordingly, we see that the final product formed in this experiment is Fe<sub>5</sub>H<sub>10</sub>P<sub>4</sub>O<sub>20</sub>, indicating that Fe<sub>5</sub>H<sub>10</sub>P<sub>4</sub>O<sub>20</sub> is evidently kinetically preferred over LiFePO<sub>4</sub>, even though the latter is still the equilibrium phase for these conditions according to the Pourbaix diagram.

Our ability to rationalize the kinetic unsuitability of certain conditions that are within the thermodynamic stability region of the Pourbaix diagram demonstrates the advantage of our MTC theory over traditional phase diagram methods.

## Discussion

We have presented here a computable thermodynamic strategy to navigate a multidimensional thermodynamic space and identify optimal experimental conditions to synthesize a phase-pure target material. Our approach adds to traditional phase diagrams a quantitative measure to approximate the kinetic competitiveness of potential competing phases. Both our large-scale analysis on text-mined synthesis recipes, and our experimental synthesis of LiIn(IO<sub>3</sub>)<sub>4</sub> and LiFePO<sub>4</sub> under varying aqueous electrochemical conditions, demonstrate that thermodynamic stability alone may not be sufficient to predict conditions that result in phase-pure synthesis. Instead, target phases are more likely to be synthesized when the energy difference

with undesired phases is maximized, such that  $\Delta\Phi$  is as negative as possible, and therefore thermodynamic competition with undesired by-products is minimized. The relevance of the quantitative competition measurement for successful synthesis is consistent with our mechanistic understanding of the kinetic processes that can bias reaction kinetics away from thermodynamic end-products. The more negative the  $\Delta\Phi$  for a target phase is, the stronger the required kinetic bias needs to be to form other phases (lower surface energy<sup>15</sup>, faster monomer diffusion or attachment rates<sup>12</sup>). As such, while the MTC does not explicitly include kinetics calculations, by minimizing the energetic competition from other phases, the MTC safeguards the synthesis of the target phases as much as possible from undesired by-products.

We note that the magnitude of the thermodynamic competition scale (tens of meV per atom) in aqueous-solution-based synthesis is smaller than the thermodynamic limit for the synthesis of metastable inorganic materials (>100 meV per atom)<sup>46</sup>, and might be comparable with DFT errors<sup>47–49</sup>. However, we note that literature-established DFT errors cannot be directly applied as error bars in our analysis because: (1) they are reduced by corrections based on the experimentally known dissolution energies of elemental solids and oxides, as implemented in pymatgen<sup>27</sup> and (2) solid-state errors in DFT tend to be systematic and to a large extent cancel between phases within the same chemistry<sup>47</sup>. Another important consideration is that the MTC analysis here predicts how  $\Delta\Phi$  between a target phase and undesired phases changes with applied aqueous electrochemical conditions. Because the gradients of the high-dimensional Pourbaix free-energy planes are formulated based on the chemical compositions of the phases, which are known exactly, this means we can evaluate  $\Delta\Phi$  with much greater confidence than  $\Phi$ .

Beyond synthesis from aqueous solutions, we note that our schema is generalizable to other synthesis scenarios. For other synthesis methods, appropriate thermodynamic potentials based on different natural intensive variables are also viable. Fortunately, Materials Genome Initiative efforts have not only led to large-scale ab initio computed databases<sup>1,3</sup> that provide reliable sources of thermodynamic data, but also deliver materials analysis platforms<sup>2</sup> that can automate competing phase-generation and grand-potential calculations. Therefore, different thermodynamic potentials can be easily constructed from this thermodynamic data using Legendre transformations based on the relevant boundary conditions of the thermodynamic system<sup>27,50</sup>. For example, the surface-energy term should be considered in nanoparticle synthesis analysis<sup>15,51,52</sup>; mechanical work should be included in ball-milling synthesis<sup>53–55</sup>; and an electromagnetic-susceptibility term is important to take into account when electric and magnetic fields are applied<sup>56,57</sup>. Thus, the MTC hypothesis can be extended to different synthesis scenarios, although the applicability of MTC in different syntheses requires further comprehensive and systematic evaluation.

## Methods

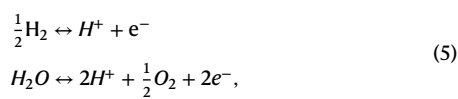
### Thermodynamic potential in an aqueous solution system

To apply the MTC hypothesis to synthesis from aqueous solutions, the relevant thermodynamic potential is the Pourbaix potential, which can be constructed from the Gibbs free energy by Legendre transformation:

$$\Phi(Y) = G - \frac{\partial G}{\partial N_{\text{H}}} N_{\text{H}} - \frac{\partial G}{\partial N_{\text{O}}} N_{\text{O}} - \frac{\partial G}{\partial Q} Q, \quad (4)$$

where  $N_{\text{M}}$ ,  $N_{\text{O}}$ ,  $N_{\text{H}}$  are the number of metal, oxygen and hydrogen atoms in the composition, respectively, and  $Q$  is the charge of the phase<sup>15</sup>. The partial derivative of  $G$  with respect to  $N_{\text{H}}$  is the chemical potential of hydrogen  $\mu_{\text{H}}$ . The partial derivative with respect to  $N_{\text{O}}$  is the chemical potential of oxygen  $\mu_{\text{O}}$ . The partial derivative with respect to  $Q$  is the redox potential  $E$ .

The two constraints imposed by equilibrium in water,



yield:

$$\begin{aligned} \mu_{\text{H}} &= \mu_{\text{H}^+} - E \\ \mu_{\text{O}} &= \mu_{\text{H}_2\text{O}} - 2\mu_{\text{H}^+} + 2E \end{aligned} \quad (6)$$

After substituting the chemical equilibrium equations from equation (6) and the relationship between pH and  $\mu_{\text{H}}$  ( $\mu_{\text{H}} = -RT \times \ln(10) \times \text{pH}$ ) into the Legendre transformation equation (4) and normalizing the Pourbaix potential by the number of metal atoms, the Pourbaix potential can be obtained:

$$\bar{\Psi} = \frac{1}{N_{\text{M}}} ((G - N_{\text{O}}\mu_{\text{H}_2\text{O}}) - RT \times \ln(10) \times (2N_{\text{O}} - N_{\text{H}}) \text{pH} - (2N_{\text{O}} - N_{\text{H}} + Q)E) \quad (7)$$

The molar Gibbs free energy of a compound,  $G$ , is its chemical potential,  $\mu_i = \mu_i^\circ + RT \ln[a_i]$ , where  $\mu_i^\circ$  is given by the standard-state Gibbs formation free energy. A pure solid with no defects has an activity of 1, making the  $RT \ln[a_i]$  term zero. The chemical potential of metal ions in solution is assumed to scale with the natural log of the metal ion concentration in solution.

### Thermodynamic competition calculation and optimization

The thermodynamic data used here were retrieved from the Materials Project<sup>3</sup> using the Python Materials Genomic (pymatgen) package<sup>2</sup>. All competing phases and corresponding Pourbaix potentials were generated and calculated through the Pourbaix Diagram module<sup>27</sup>. Here we assume that the thermodynamic potential is linearized<sup>15</sup>, such that the thermodynamic competition analysis formulated in equation (1) can be treated as a convex optimization problem in its natural variables, as stated by the pointwise minimum theorem<sup>58</sup>. Therefore, gradient-based optimization algorithms (Code availability and Supplementary Information Note 1) can be used to optimize natural variables (that is, pH, redox potential ( $E$ ), and log-scaled concentrations ( $\ln[X]$ ) in aqueous solution system) to obtain the minimized thermodynamic competition in the pre-defined searching synthesis space. In this work, the searching synthesis space was defined as  $0 \leq \text{pH} \leq 14$ ,  $-1\text{V} \leq E \leq 2\text{V}$  and  $0 \text{ mol l}^{-1} \leq [X] \leq 2 \text{ mol l}^{-1}$ .

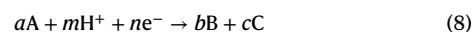
### Text-mined dataset analysis

We used the dataset of text-mined solution-based synthesis recipes<sup>22</sup> to perform the thermodynamic competition analysis. We first filtered out syntheses that have a final heat-treatment step after the precipitate is obtained from the solution. Then, we identified aqueous solution syntheses based on the solvent (that is, solvent is water)<sup>22</sup>. The filtering resulted in 20,062 out of 35,675 procedures to be defined as aqueous-solution-based without subsequent heat treatment. In this subset, 4,431 unique targets were synthesized, and 1,370 of them can be found in the Materials Project database, leading to 421 metal oxides and 251 unique polyanionic compounds. We selected procedures resulting in ternary metal oxides, phosphates, carbonates, iodates, sulfates and silicates, as synthesized targets, and kept only those targets with an mp-id, meaning their thermodynamic data are available in the Materials Project database. Because the dataset is unbalanced, we randomly sampled up to three procedures for compounds, such as  $\text{LiFePO}_4$  and  $\text{CaCO}_3$ , which appear with high frequency to avoid distributions being skewed. To specify the synthesis conditions, we manually curated the synthesis recipes: (1) the quantities of materials were converted into concentrations of different ions; (2) pH was calculated based on the concentrations and  $\text{p}K_{\text{a}}$  of different ions using pHcalc (<https://github.com/rnelsonchem/pHcalc>); (3) the redox potentials at the calculated pH

were estimated. We only kept synthesis recipes that can provide enough information to construct the Pourbaix system. In the final dataset used for the statistical analysis in Fig. 2, there are 139 unique ternary metal oxides, 40 phosphates, 15 carbonates, 13 iodates, 9 sulfates and 9 silicates. Pourbaix potentials for all target phases and their corresponding possible competing phases were then calculated based on the estimated synthesis conditions using the Pourbaix diagram module in pymatgen. Finally, we calculated the thermodynamic competition the target phases experience according to equation (1). We then performed the optimization to minimize the thermodynamic competition the target phases experience from competing phases for comparison purposes. The details of the data format are provided in Supplementary Information Note 3.

### Effective electrochemical potential of redox agents

The half-cell reaction between an oxidized species [A] and its reduced product [B] can be written as:



The effective electrochemical redox potential of these redox pairs is determined by the Nernst equation:

$$E = E^\ominus - 0.0591 \frac{1}{n} \ln \frac{[\text{B}]^b [\text{C}]^c}{[\text{A}]^a} - 0.0591 \frac{m}{n} \text{pH} \quad (9)$$

Here, A and B represent the redox pair, C is another possible chemical species involved in the reaction in case A and B cannot form a balanced reaction, and  $E^\ominus$  is the standard redox potential.

We note that after the product phase has nucleated and the reaction proceeds via crystal growth, the chemical oxidizing/reducing agents will be consumed, and the effective electrochemical redox potential in the solution will change as a function of reaction progress. Determining the final redox potential and pH of an aqueous synthesis reaction is not currently amenable to Pourbaix diagram analyses because this requires a model to couple the growth of the solid phase to the depletion of the solution. Based on refs. 59,60, we use the following formula to estimate the redox potential in the system:

$$E = E^\ominus - 0.0591 \frac{m}{n} \text{pH} \quad (10)$$

### Synthesis of $\text{LiIn}(\text{IO}_3)_4$

$\text{Li}(\text{CH}_3\text{COO})$  (anhydrous, Sigma-Aldrich, 99.9%) and  $\text{LiCl}$  (Sigma-Aldrich, 99%) were used as lithium sources for the synthesis of  $\text{LiIn}(\text{IO}_3)_4$ . Different amounts of lithium salts (A1, 1.5 mmol  $\text{Li}(\text{CH}_3\text{COO}) + 13.5$  mmol  $\text{LiCl}$ ; A2, 15 mmol  $\text{LiCl}$ ; A3, 1.5 mmol  $\text{Li}(\text{CH}_3\text{COO}) + 10.5$  mmol  $\text{LiCl}$ ; A4, 12 mmol  $\text{LiCl}$ ; A5, 1.5 mmol  $\text{Li}(\text{CH}_3\text{COO}) + 6.5$  mmol  $\text{LiCl}$ ; A6, 8 mmol  $\text{LiCl}$ ; A7, 1.5 mmol  $\text{Li}(\text{CH}_3\text{COO}) + 3.5$  mmol  $\text{LiCl}$ ; A8, 5 mmol  $\text{LiCl}$ ; A9, 1.5 mmol  $\text{Li}(\text{CH}_3\text{COO})$ ; and A10, 1.5 mmol  $\text{LiCl}$ ) were mixed with 0.5 mmol  $\text{In}_2\text{O}_3$  and 8 mmol  $\text{H}_3\text{IO}_6$ . The mixture was dissolved in 10 ml water. The obtained solution was sealed in an autoclave equipped with a Teflon liner (49 ml) and heated at 200 °C for 132 h, followed by natural cooling to room temperature. The products were centrifuged, washed with water three times and dried in a 70 °C vacuum oven for 12 h.

### Synthesis of $\text{LiFePO}_4$

$\text{LiFePO}_4$  was synthesized by a hydrothermal method in a nitrogen environment. This method involved dissolving 5 mmol  $\text{FeSO}_4 \cdot 7\text{H}_2\text{O}$  (Sigma-Aldrich, 99%), 15 mmol  $\text{LiOH} \cdot \text{H}_2\text{O}$  (Sigma-Aldrich, 99.95%), 0.04 g sucrose and various amounts of 85 wt%  $\text{H}_3\text{PO}_4$  (Sigma-Aldrich) in 20 ml water and then sealing the solution in an autoclave equipped with a Teflon liner (49 ml). The pH of the mixture solution was controlled by the amount of 85 wt%  $\text{H}_3\text{PO}_4$ . The autoclave was heated at 170 °C for 12 h, followed by natural cooling to room temperature. The products were centrifuged, washed with water and ethanol three times and dried in a 70 °C vacuum oven for 12 h.



## Structure characterization

X-ray diffraction analysis was carried out using a Rigaku MiniFlex 600 diffractometer with Cu K $\alpha$  radiation ( $\lambda = 1.5406 \text{ \AA}$ ) with a step size of  $1^\circ \text{ min}^{-1}$  from  $10^\circ$  to  $70^\circ$ .

## Data availability

All relevant data are provided within this paper and are available at <https://doi.org/10.6084/m9.figshare.23902362> ref. 61,42.

## Code availability

All of the codes used for analysing the coordination environment were based on pymatgen software and its Pourbaix diagrams module<sup>27</sup>. Code to calculate the thermodynamic competition and optimize synthesis conditions by minimizing thermodynamic competition is provided at: [https://github.com/zherenwang/synthesis\\_condition\\_optimizer](https://github.com/zherenwang/synthesis_condition_optimizer).

## References

1. Holden, J. *Materials Genome Initiative for Global Competitiveness* (National Science and Technology Council, 2011).
2. Ong, S. P. et al. Python materials genomics (pymatgen): a robust, open-source python library for materials analysis. *Comput. Mater. Sci.* **68**, 314–319 (2013).
3. Jain, A. et al. Commentary: The Materials Project: a materials genome approach to accelerating materials innovation. *APL Mater.* **1**, 011002 (2013).
4. Curtarolo, S. et al. The high-throughput highway to computational materials design. *Nat. Mater.* **12**, 191–201 (2013).
5. Sumpter, B. G., Vasudevan, R. K., Potok, T. & Kalinin, S. V. A bridge for accelerating materials by design. *NPJ Comput. Mater.* **1**, 15008 (2015).
6. Kohlmann, H. Looking into the black box of solid-state synthesis. *Eur. J. Inorg. Chem.* **2019**, 4174–4180 (2019).
7. Chamorro, J. R. & McQueen, T. M. Progress toward solid state synthesis by design. *Accs. Chem. Res.* **51**, 2918–2925 (2018).
8. Walters, L. N., Zhang, C., Dravid, V. P., Poeppelmeier, K. R. & Rondinelli, J. M. First-principles hydrothermal synthesis design to optimize conditions and increase the yield of quaternary heteroanionic oxychalcogenides. *Chem. Mater.* **33**, 2726–2741 (2021).
9. Zhao, Y. et al. Pourbaix diagram for Hp-<sup>13</sup>Cr stainless steel in the aggressive oilfield environment characterized by high temperature, high CO<sub>2</sub> partial pressure and high salinity. *Electrochim. Acta* **293**, 116–127 (2019).
10. Huang, L. F., Hutchison, M. J., Santucci, R. J., Scully, J. R. & Rondinelli, J. M. Improved electrochemical phase diagrams from theory and experiment: the Ni–water system and its complex compounds. *J. Phys. Chem. C* **121**, 9782–9789 (2017).
11. Huang, L.-F., Ha, H. M., Lutton Cwalina, K., Scully, J. R. & Rondinelli, J. M. Understanding electrochemical stabilities of Ni-based nanofilms from a comparative theory–experiment approach. *J. Phys. Chem. C* **123**, 28925–28940 (2019).
12. Bianchini, M. et al. The interplay between thermodynamics and kinetics in the solid-state synthesis of layered oxides. *Nat. Mater.* **19**, 1088–1095 (2020).
13. Bai, J. et al. Kinetic pathways templated by low-temperature intermediates during solid-state synthesis of layered oxides. *Chem. Mater.* **32**, 9906–9913 (2020).
14. Wang, Y., He, J., Liu, C., Chong, W. H. & Chen, H. Thermodynamics versus kinetics in nanosynthesis. *Angew. Chem. Inter. Ed.* **54**, 2022–2051 (2015).
15. Sun, W., Kitchaev, D. A., Kramer, D. & Ceder, G. Non-equilibrium crystallization pathways of manganese oxides in aqueous solution. *Nat. Commun.* **10**, 573 (2019).
16. Chen, B.-R. et al. Understanding crystallization pathways leading to manganese oxide polymorph formation. *Nat. Commun.* **9**, 2553 (2018).
17. Balluffi, R., Allen, S. & Carter, W. in *Kinetics of Materials* (eds R.W. Balluffi et al.) Chap. 21 (Wiley, 2005).
18. Hoffman, J. D. Thermodynamic driving force in nucleation and growth processes. *J. Chem. Phys.* **29**, 1192–1193 (1958).
19. Whitman, J. R., Aranovich, G. L. & Donohue, M. D. Thermodynamic driving force for diffusion: comparison between theory and simulation. *J. Chem. Phys.* **134**, 094303 (2011).
20. Walters, L. N., Wang, E. L. & Rondinelli, J. M. Thermodynamic descriptors to predict oxide formation in aqueous solutions. *J. Phys. Chem. Lett.* **13**, 6236–6243 (2022).
21. Sun, W. & Powell-Palm, M. J. Generalized Gibbs' phase rule. Preprint at <https://arxiv.org/abs/2105.01337> (2021).
22. Wang, Z. et al. Dataset of solution-based inorganic materials synthesis procedures extracted from the scientific literature. *Sci. Data* **9**, 231 (2022).
23. Patel, A. M., Nørskov, J. K., Persson, K. A. & Montoya, J. H. Efficient Pourbaix diagrams of many-element compounds. *Phys. Chem. Chem. Phys.* **21**, 25323–25327 (2019).
24. Navrotsky, A. Energetic clues to pathways to biomineralization: precursors, clusters, and nanoparticles. *Proc. Natl Acad. Sci. USA* **101**, 12096–12101 (2004).
25. Sun, W., Jayaraman, S., Chen, W., Persson, K. A. & Ceder, G. Nucleation of metastable aragonite CaCO<sub>3</sub> in seawater. *Proc. Natl Acad. Sci. USA* **112**, 3199–3204 (2015).
26. Kitchaev, D. A. & Ceder, G. Evaluating structure selection in the hydrothermal growth of FeS<sub>2</sub> pyrite and marcasite. *Nat. Commun.* **7**, 13799 (2016).
27. Persson, K. A., Waldwick, B., Lazic, P. & Ceder, G. Prediction of solid–aqueous equilibria: scheme to combine first-principles calculations of solids with experimental aqueous states. *Phys. Rev. B* **85**, 235438 (2012).
28. Jia, X. et al. Anthropogenic biases in chemical reaction data hinder exploratory inorganic synthesis. *Nature* **573**, 251–255 (2019).
29. Kharissova, O. V., Kharisov, B. I., Oliva González, C. M., Méndez, Y. P. & López, I. Greener synthesis of chemical compounds and materials. *R. Soc. Open Sci.* **6**, 191378 (2019).
30. Hautier, G., Ong, S. P., Jain, A., Moore, C. J. & Ceder, G. Accuracy of density functional theory in predicting formation energies of ternary oxides from binary oxides and its implication on phase stability. *Phys. Rev. B* **85**, 155208 (2012).
31. Sun, W. et al. The thermodynamic scale of inorganic crystalline metastability. *Science Advances* **2**, e1600225 (2016).
32. Gopalakrishnan, J. Chimie douce approaches to the synthesis of metastable oxide materials. *Chem. Mater.* **7**, 1265–1275 (1995).
33. Martin, S. T. in *Environmental Catalysis* (ed. Grassian, V. H.) Ch. 4 (Taylor & Francis, 2005).
34. Murray, J. W., Dillard, J. G., Giovanoli, R., Moers, H. & Stumm, W. Oxidation of Mn(II): initial mineralogy, oxidation state and ageing. *Geochim. Cosmochim. Acta* **49**, 463–470 (1985).
35. Huo, H. et al. Machine-learning rationalization and prediction of solid-state synthesis conditions. *Chem. Mater.* **34**, 7323–7336 (2022).
36. David, N., Sun, W. & Coley, C. W. The promise and pitfalls of AI for molecular and materials synthesis. *Nat. Comput. Sci.* **3**, 362–364 (2023).
37. Jun, K. et al. Lithium superionic conductors with corner-sharing frameworks. *Nat. Mater.* **21**, 924–931 (2022).
38. Manthiram, A. & Goodenough, J. Lithium insertion into Fe<sub>2</sub>(SO<sub>4</sub>)<sub>3</sub> frameworks. *J. Power Sources* **26**, 403–408 (1989).
39. Yang, B.-P., Sun, C.-F., Hu, C.-L. & Mao, J.-G. A series of new alkali metal indium iodates with isolated or extended anions. *Dalton Trans.* **40**, 1055–1060 (2011).
40. Pourbaix, M. *Atlas of Electrochemical Equilibria in Aqueous Solution* (NACE, 1974).

41. Mills, A., Hazafy, D., Elouali, S. & O'Rourke, C. Periodate—an alternative oxidant for testing potential water oxidation catalysts. *J. Mater. Chem. A* **4**, 2863–2872 (2016).
42. Zagorac, D., Müller, H., Ruehl, S., Zagorac, J. & Rehme, S. Recent developments in the Inorganic Crystal Structure Database: theoretical crystal structure data and related features. *J. Appl. Crystallogr.* **52**, 918–925 (2019).
43. Singh, A. K., Montoya, J. H., Gregoire, J. M. & Persson, K. A. Robust and synthesizable photocatalysts for CO<sub>2</sub> reduction: a data-driven materials discovery. *Nat. Commun.* **10**, 443 (2019).
44. Liu, J., Jiang, R., Wang, X., Huang, T. & Yu, A. The defect chemistry of LiFePO<sub>4</sub> prepared by hydrothermal method at different pH values. *J. Power Sources* **194**, 536–540 (2009).
45. Schröder, U. Anodic electron transfer mechanisms in microbial fuel cells and their energy efficiency. *Phys. Chem. Chem. Phys.* **9**, 2619–2629 (2007).
46. Aykol, M., Dwaraknath, S. S., Sun, W. & Persson, K. A. Thermodynamic limit for synthesis of metastable inorganic materials. *Sci. Adv.* **4**, eaaq0148 (2018).
47. Bartel, C. J. et al. A critical examination of compound stability predictions from machine-learned formation energies. *NPJ Comput. Mater.* **6**, 97 (2020).
48. Wang, L., Maxisch, T. & Ceder, G. Oxidation energies of transition metal oxides within the GGA+U framework. *Phys. Rev. B* **73**, 195107 (2006).
49. Gong, S. et al. Calibrating DFT formation enthalpy calculations by multifidelity machine learning. *JACS Au* **2**, 1964–1977 (2022).
50. Ong, S. P., Wang, L., Kang, B. & Ceder, G. Li–Fe–P–O<sub>2</sub> phase diagram from first principles calculations. *Chem. Mater.* **20**, 1798–1807 (2008).
51. Navrotsky, A., Mazeina, L. & Majzlan, J. Size-driven structural and thermodynamic complexity in iron oxides. *Science* **319**, 1635–1638 (2008).
52. Ranade, M. R. et al. Energetics of nanocrystalline TiO<sub>2</sub>. *Proc. Natl Acad. Sci. USA* **99**, 6476–6481 (2002).
53. Yang, L., Moores, A., Friščić, T. & Provatas, N. Thermodynamics model for mechanochemical synthesis of gold nanoparticles: implications for solvent-free nanoparticle production. *ACS Appl. Nano Mater.* **4**, 1886–1897 (2021).
54. Rana, R. et al. Insights into the mechanism of the mechanochemical formation of metastable phases. *ACS Appl. Mater. Interfaces* **13**, 6785–6794 (2021).
55. Tricker, A. W., Samaras, G., Heibisch, K. L., Realf, M. J. & Sievers, C. Hot spot generation, reactivity, and decay in mechanochemical reactors. *Chem. Eng. J.* **382**, 122954 (2020).
56. Aber, J. E., Arnold, S., Garetz, B. A. & Myerson, A. S. Strong DC electric field applied to supersaturated aqueous glycine solution induces nucleation of the  $\gamma$  polymorph. *Phys. Rev. Lett.* **94**, 145503 (2005).
57. Potticary, J. et al. An unforeseen polymorph of coronene by the application of magnetic fields during crystal growth. *Nat. Commun.* **7**, 11555 (2016).
58. Boyd, S. & Vandenberghe, L. *Convex Optimization* (Cambridge Univ. Press, 2004).
59. Parent, A. R., Crabtree, R. H. & Brudvig, G. W. Comparison of primary oxidants for water-oxidation catalysis. *Chem. Soc. Rev.* **42**, 2247–2252 (2013).
60. Wasylenko, D. J. et al. Electronic modification of the [Ru<sup>II</sup>(tpy)(bpy)(OH<sub>2</sub>)<sup>2+</sup>] scaffold: effects on catalytic water oxidation. *J. Am. Chem. Soc.* **132**, 16094–16106 (2010).
61. Wang, Z. et al. Text-mined synthesis dataset used in optimal thermodynamic conditions to minimize kinetic byproducts in aqueous materials synthesis (2023); <https://doi.org/10.6084/m9.figshare.23902362>

## Acknowledgements

Work by Z.W., Y.S., T.H. and G.C. was supported by the National Science Foundation under grant number DMR-1922372. Work by K.C. was funded by the US Department of Energy, Office of Science, Office of Basic Energy Sciences, Materials Sciences and Engineering Division under contract number DE-AC02-05-CH11231 (D2S2 program KCD2S2). Work by Y.Z. and Y.F. was supported by the Laboratory Directed Research and Development Program of Lawrence Berkeley National Laboratory under US Department of Energy contract number DE-AC02-05CH11231 (FY23 LDRD 23-128). Work by K.J. was supported by the Assistant Secretary for Energy Efficiency and Renewable Energy, Vehicle Technologies Office, of the US Department of Energy under contract number DE-AC02-05CH11231, under the Advanced Battery Materials Research (BMR) Program (CPS 35950). W.S. was supported by the National Science Foundation under grant number NSF DMR-2240281.

## Author contributions

Z.W., W.S. and G.C. conceived the idea. Z.W., W.S., Z.L. and J.S. formulated the thermodynamic competition metric. Y.S., Y.F. and Y.Z. performed experiments. Y.-W.B. created the experimental platform. Z.W., K.C., Y.F. and T.H. processed the text-mined dataset. Z.W., K.C., Y.F., W.S. and G.C. performed analysis on the text-mined dataset. Z.W., Y.S., Y.Z. and K.J. analysed the experimental data. Z.W., Y.S., W.S. and G.C. drafted the paper. G.C. supervised the project. All authors discussed the results and contributed to the final paper.

## Competing interests

The authors declare no competing interests.

## Additional information

**Supplementary information** The online version contains supplementary material available at <https://doi.org/10.1038/s44160-023-00479-0>.

**Correspondence and requests for materials** should be addressed to Wenhao Sun or Gerbrand Ceder.

**Peer review information** *Nature Synthesis* thanks Jonathan Scragg and the other, anonymous, reviewer(s) for their contribution to the peer review of this work. Primary Handling Editor: Peter Seavill, in collaboration with the *Nature Synthesis* team

**Reprints and permissions information** is available at [www.nature.com/reprints](http://www.nature.com/reprints).

**Publisher's note** Springer Nature remains neutral with regard to jurisdictional claims in published maps and institutional affiliations.

**Open Access** This article is licensed under a Creative Commons Attribution 4.0 International License, which permits use, sharing, adaptation, distribution and reproduction in any medium or format, as long as you give appropriate credit to the original author(s) and the source, provide a link to the Creative Commons license, and indicate if changes were made. The images or other third party material in this article are included in the article's Creative Commons license, unless indicated otherwise in a credit line to the material. If material is not included in the article's Creative Commons license and your intended use is not permitted by statutory regulation or exceeds the permitted use, you will need to obtain permission directly from the copyright holder. To view a copy of this license, visit <http://creativecommons.org/licenses/by/4.0/>.

© The Author(s) 2024